



ACADEMIC
PRESS

Available online at www.sciencedirect.com

SCIENCE @ DIRECT®

Journal of Computational Physics 184 (2003) 299–320

JOURNAL OF
COMPUTATIONAL
PHYSICS

www.elsevier.com/locate/jcp

A study of the effects of grid non-orthogonality on the solution of shallow water equations in boundary-fitted coordinate systems

S. Sankaranarayanan^{a,*}, Malcolm L. Spaulding^b

^a *Applied Science Associates, 70, Dean Knauss Drive, Narragansett, RI 02882, USA*

^b *Ocean Engineering, University of Rhode Island, Narragansett, RI 02882, USA*

Received 28 November 2001; received in revised form 11 October 2002; accepted 23 October 2002

Abstract

In the present study, an existing two-dimensional boundary-fitted model [J. Hydraul. Eng.-ASCE 122 (9) (1996) 512] is used to study the effect of grid non-orthogonality on the solution of shallow water equations using boundary-fitted grids. The linearized two-dimensional shallow water equations are expressed in terms of the grid angle and aspect ratio. The truncation errors of the finite difference approximations used in the solution of the governing equations are shown to be dependent on the grid angle and the aspect ratio. The coefficient of the truncation error was shown to increase, with the decrease in the grid angle. The RMS errors in model predicted surface elevations and velocities for the case of seiche in a rectangular basin are found to increase gradually, as the grid resolution decreases from 174 to 80 gridpoints per wavelength or as the grid angle decreases from 90° to 50° and increases rather sharply for a grid angle of 30° at grid resolutions less than 80 gridpoints per wavelength. The model predicted surface elevations for the case of tidal forcing in a rectangular basin are found to be insensitive to the grid angle at grid resolutions higher than 600 gridpoints per wavelength. The RMS error in the model predicted velocities is found to increase gradually as the grid angle decreases from 90° to 30° or as the grid resolution decreases from 1400 gridpoints per wavelength to 400 gridpoints per wavelength and increases sharply as the grid resolution decreases from 400 to 150 gridpoints per wavelength. Two-dimensional depth averaged hydrodynamic modeling of tidal circulation in Narragansett Bay, using three different boundary-fitted grids showed that the model predicted surface elevations are insensitive to the grid angle at grid resolutions as low as 200 gridpoints per wavelength. However, the model predicted velocities were found to increase as the grid resolution decreases from 600 to 200 gridpoints per wavelength. We conclude from this study that grid angle and grid resolution affects the accuracy of the model predicted currents and the numerical dispersion increases with the decrease in grid angle or grid resolution and these are in agreement with that reached by Sankaranarayanan and Spaulding [Dispersion and Stability Analyses of Shallow Water Equations in Boundary-fitted Coordinates, Department of Ocean Engineering, University of Rhode Island, 2001, p. 33] through a Fourier analysis of the discretized equations in boundary-fitted coordinates.

© 2002 Elsevier Science B.V. All rights reserved.

* Corresponding author.

E-mail addresses: sankar@appsci.com, subbayya@appsci.com (S. Sankaranarayanan), spaulding@oce.uri.edu (M.L. Spaulding).

¹ Formerly at Ocean Engineering, University of Rhode Island, USA.

Keywords: Non-orthogonality; Boundary-fitted grids; Truncation error

Nomenclature

ζ	water elevation
ϕ, θ	spherical coordinate system
ρ	density of water
g	gravitation
ξ, η	generalized curvilinear coordinate system
D	elevation + water depth ($D = h + \zeta$)
h	water depth
L	wavelength
l	length of channel
R	radius of earth
T	wave period
U, V	vertically averaged velocities in ϕ - and θ -directions, respectively
U^c, V^c	vertically averaged velocities in ξ - and η -directions, respectively

1. Introduction

Accurate prediction of tidal elevations and currents is essential for modeling the salinity distribution and dispersion of pollutants in bays. Since the geometry and bathymetry of water bodies are quite complex, traditional finite difference methods, using rectangular grids, require very fine grids to resolve the shoreline and small coves, resulting in a substantial increase in computational effort. To address some of the limitations of the traditional finite difference methods, conformal grids [3] and orthogonal curvilinear grids [4] were used to model water bodies with less complicated geometries. However, it is relatively difficult to generate conformal and orthogonal curvilinear grids for water bodies having narrow coves and tidal inlets. The topography and bathymetry of the study area can be represented better with the minimum number of gridpoints using a non-orthogonal grid. Numerical hydrodynamic models using generalized non-orthogonal, boundary-fitted grids [5–7] were used to overcome the limitations of models using orthogonal and conformal grids. The generation of the boundary-fitted grids is usually based on the solution of homogeneous or non-homogeneous elliptic partial differential equations, which can be solved by standard finite difference methods [8]. The governing flow equations need to be transformed to the curvilinear coordinates, so that they can be solved on a boundary-fitted grid. In [6,7,9], they transformed only the independent variables (coordinate geometry) in the governing equations. Due to difficulties in satisfying lateral boundary conditions, Muin and Spaulding [1] and Borthwick and Akponasa [10] transformed both the dependent (components of velocities) and the independent variables. Muin and Spaulding [1] extended Sheng's [5] approach to spherical coordinates. The equations of motion in spherical coordinates, expressed in terms of contravariant velocities, were solved on a non-orthogonal boundary-fitted grid [1].

The choice of a given boundary-fitted grid configuration can have a substantial impact on the numerical solution of the governing equations [8,11]. When the transformed governing equations are solved using finite difference methods, the truncation error of the finite difference expressions used depends on: (i) the higher-order derivatives of the solution variables, (ii) the rate of change of grid spacing, and (iii) the non-orthogonality of the grid. Thompson et al. [8], Kerlick and Klopfer [12], and Mastin [11] showed using truncation error analysis, that the error due to grid non-orthogonality is small, if the grid angle is not less than 45°. Nielson and Skovgaard [13] went on to verify Thompson et al. [8] result by solving the linearized shallow water equations in (i) the region between two concentric cylinders and (ii) a non-rotating parabolic

container, where the surface is not necessarily a plane. It is noted that Nielsen and Skovgaard [13] did not transform the dependent variables (velocities) in their solution methodology.

Lee and Tsuei [14] computed the truncation errors of convective terms of the Navier–Stokes equation in a curvilinear coordinate system. They concluded that the optimal grid arrangement strongly depended on the flow field and hence suggested the use of grid adaptation based on the flow field, to minimize the truncation error.

Sankaranarayanan and Spaulding [2], through a Fourier analysis of the discretized equations in boundary-fitted coordinates, showed that the dispersivity increases with a decrease in grid angle or grid resolution.

In the present study, the model developed by Muin and Spaulding [1] is used to evaluate the effect of grid angle on the numerical solution of shallow water equations in a generalized, non-orthogonal, boundary-fitted coordinate system. A truncation error analysis of the finite difference approximations is performed and expressed in terms of grid quality parameters, specifically the grid aspect ratio and the grid angle. Grid configurations with different grid angles and aspect ratios are generated and used to test the effect of grid angle on the model predicted surface elevations and velocities to select problems. Systematic studies on the effects of grid skewness in the model predicted velocities were clearly absent in the earlier studies [13].

2. Governing equations

Using a spherical coordinate system, where ϕ is the longitude, θ is the latitude, R is the radius of the earth, the two-dimensional vertically averaged continuity equation is given by [1]

$$\frac{\partial \zeta}{\partial t} + \frac{1}{R \cos \theta} \frac{\partial UD}{\partial \phi} + \frac{1}{R} \frac{\partial VD}{\partial \theta} - \frac{VD}{R} \tan \theta = 0, \quad (1)$$

where U and V are the vertically averaged velocities in the ϕ - and θ -directions, respectively, R is the mean radius of the earth, ζ is the water surface elevation, D is the total depth ($\zeta + h$), and h is the water depth.

Coriolis effects have been neglected and hence our analysis will be applicable to small- and mesoscale problems where Rossby number $R_0 = V/(2\Omega L_s) \gg 1$, where V and L_s are the velocity and length scales of the motion, respectively, and Ω denotes the angular velocity of the earth; cf. [24, Chapter 1.2]. The non-linear advection terms are neglected, to make a simple and meaningful analysis of the effects of grid skewness on the solution.

Neglecting the advective, viscous, and Coriolis terms, the momentum equation in the ϕ -direction is given by

$$\frac{\partial UD}{\partial t} = -\frac{gD}{R \cos \theta} \left(\frac{\partial \zeta}{\partial \phi} \right) - \frac{\tau_{b\phi}}{\rho}. \quad (2)$$

Similarly, the momentum equation in the θ -direction is given by

$$\frac{\partial VD}{\partial t} = -\frac{gD}{R} \left(\frac{\partial \zeta}{\partial \theta} \right) - \frac{\tau_{b\theta}}{\rho}, \quad (3)$$

where $\tau_{b\phi} = \rho C_b U \sqrt{U^2 + V^2}$, $\tau_{b\theta} = \rho C_b V \sqrt{U^2 + V^2}$, C_b is the bed friction coefficient, ρ is the density of water, and g is the acceleration due to gravity.

2.1. Governing equations in the curvilinear coordinate system

The linearized, transformed equations of motion, in terms of the contravariant velocities (U^c and V^c) in the curvilinear coordinate system ξ, η , are given by

Continuity equation:

$$\frac{\partial \zeta}{\partial t} + \frac{1}{R \cos \theta} \frac{1}{J} \left[(JU^c \cos \theta D)_\xi + (JV^c \cos \theta D)_\eta \right] = 0, \tag{4}$$

Momentum equation in ϕ -direction:

$$\frac{\partial (DU^c)}{\partial t} = - \frac{gD(\theta_\eta \theta_\eta + \phi_\eta \phi_\eta \cos^2 \theta)}{J^2 R \cos^2 \theta} \zeta_\xi + \frac{gD(\theta_\xi \theta_\eta + \phi_\xi \phi_\eta \cos^2 \theta)}{J^2 R \cos^2 \theta} \zeta_\eta - \frac{\tau_{b\phi}^c}{\rho}, \tag{5}$$

Momentum equation in θ -direction:

$$\frac{\partial (DV^c)}{\partial t} = \frac{gD(\phi_\eta \phi_\xi \cos^2 \theta + \theta_\xi \theta_\eta)}{J^2 R \cos^2 \theta} \zeta_\xi - \frac{gD(\phi_\xi \phi_\xi \cos^2 \theta + \theta_\xi \theta_\xi)}{J^2 R \cos^2 \theta} \zeta_\eta - \frac{\tau_{b\theta}^c}{\rho} \tag{6}$$

and the subscripted variables ($\phi_\xi, \phi_\eta, \theta_\xi$ and θ_η) refer to derivatives with respect to the subscripts indicated. J is the Jacobian given by, $J = \phi_\xi \theta_\eta - \phi_\eta \theta_\xi$. The relationship between the contravariant vertically averaged velocities (U^c, V^c) and velocities in spherical coordinates (U, V) is given by

$$\begin{aligned} U &= \cos \theta \phi_\xi U^c + \cos \theta \phi_\eta V^c, \\ V &= \theta_\xi U^c + \theta_\eta V^c. \end{aligned} \tag{7}$$

The bottom stress terms in the contravariant form, $\tau_{b\phi}^c$ and $\tau_{b\theta}^c$, can be written as

$$\tau_{b\phi}^c = \rho C_b U^c \sqrt{(U^c)^2 + (V^c)^2}, \quad \tau_{b\theta}^c = \rho C_b V^c \sqrt{(U^c)^2 + (V^c)^2}.$$

2.2. Governing equations in terms of grid quality parameters

The position vector on the surface of the sphere ($\phi, \theta, R = \text{constant}$) is given by

$$\hat{r} = R \cos \theta \phi \hat{e}_\phi + R \theta \hat{e}_\theta, \tag{8}$$

where \hat{e}_ϕ and \hat{e}_θ are the curvilinear vectors in the ϕ - and θ -directions, respectively.

The derivatives of the position vectors in the (ξ, η) -directions are given by

$$\hat{g}_1 = \frac{\partial \hat{r}}{\partial \xi} = R \cos \theta \phi_\xi \hat{e}_\xi + R \theta_\xi \hat{e}_\eta, \tag{9}$$

$$\hat{g}_2 = \frac{\partial \hat{r}}{\partial \eta} = R \cos \theta \phi_\eta \hat{e}_\xi + R \theta_\eta \hat{e}_\eta, \tag{10}$$

where \hat{e}_ξ and \hat{e}_η are the unit vectors in ξ, η -directions, respectively, and the subscripts in the equations indicate partial derivatives (e.g. $\phi_\xi = \partial \phi / \partial \xi$). Normalizing with respect to R , since R is constant on the surface of a sphere, the covariant components of the metric tensor $g_{ij} = \hat{g}_i \cdot \hat{g}_j$ are given by

$$g^{(ij)} = \begin{bmatrix} \phi_\xi \phi_\xi \cos^2 \theta + \theta_\xi \theta_\xi & \phi_\xi \phi_\eta \cos^2 \theta + \theta_\xi \theta_\eta \\ \phi_\xi \phi_\eta \cos^2 \theta + \theta_\xi \theta_\eta & \phi_\eta \phi_\eta \cos^2 \theta + \theta_\eta \theta_\eta \end{bmatrix}. \tag{11}$$

The angle of grid non-orthogonality (γ) or angle of the grid (Fig. 1), as it is called from now on, can be defined as

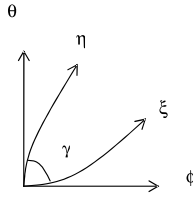


Fig. 1. Definition sketch.

$$\cos \gamma = \frac{g_{(12)}}{\sqrt{g_{(11)}g_{(22)}}}. \tag{12}$$

The Aspect Ratio (A), which measures the degree of distortion of the grid, can be defined as

$$A = \sqrt{\frac{g_{(22)}}{g_{(11)}}}, \tag{13}$$

where $g_{(ij)}$ is the metric tensor and is given by Eq. (11).

Eq. (12) can also be written as

$$\sin \gamma = \sqrt{\frac{g_{(11)}g_{(22)} - g_{(12)}^2}{g_{(11)}g_{(22)}}} = \frac{J \cos \theta}{\sqrt{g_{(11)}g_{(22)}}} \tag{14}$$

since $g_{(11)}g_{(22)} - g_{(12)}^2 = J^2 \cos^2 \theta$.

Eq. (14) can also be written, using Eq. (13), as

$$\sin \gamma = \frac{J \cos \theta}{A g_{(11)}} = \frac{JA \cos \theta}{g_{(22)}}. \tag{15}$$

Following Kerlick and Klopfer [12], the elements of the metric tensor can thus be written in terms of γ and A as

$$g_{(11)} = \frac{J \cos \theta}{A \sin \gamma}, \quad g_{(22)} = \frac{JA \cos \theta}{\sin \gamma}, \quad g_{(12)} = \cos \gamma \sqrt{g_{(11)}g_{(22)}}. \tag{16}$$

The momentum equations can now be written in terms of the grid quality parameters, the interior grid angle (γ) and the Aspect Ratio (A), as

ξ -momentum equation:

$$\frac{\partial(DU^c)}{\partial t} = -\frac{gD}{R \sin^2 \gamma g_{(11)}} \zeta_\xi + \frac{gDA \cos \gamma}{R \sin^2 \gamma g_{(22)}} \zeta_\eta, \tag{17}$$

η -momentum equation:

$$\frac{\partial(DV^c)}{\partial t} = \frac{gD \cos \gamma}{AR \sin^2 \gamma g_{(11)}} \zeta_\xi - \frac{gD}{R \sin^2 \gamma g_{(22)}} \zeta_\eta. \tag{18}$$

Eqs. (17) and (18) reduce to that for a orthogonal coordinate system for $\gamma = 90^\circ$. Additional substitutions, $g_{(11)} = g_{(22)} = R = A = 1$, reduces Eqs. (17) and (18) to that for a Cartesian coordinate system. It can be seen from Eqs. (17) and (18) that the coefficients of the four barotropic terms increase with decrease in grid angle.

3. Truncation error analysis

The transformed equations can be approximated by finite difference expressions. The spatial discretization is based on a space staggered C-grid system [16]. This analysis assumes that the spatial discretization is uniform, throughout the domain. Time derivative terms are discretized using a second-order accurate, three-level scheme [1]. The finite difference expression for a typical time derivative term is given by

$$\frac{\partial f}{\partial t} = \frac{1.5(f)_{ij}^{n+1} - 2.0(f)_{ij}^n + 0.5(f)_{ij}^{n-1}}{\Delta t} - \frac{\Delta t^2}{3} \left(\frac{\partial^3 f}{\partial t^3} \right). \tag{19}$$

The central difference expression for first-order spatial derivatives is given by

$$\frac{\partial f}{\partial \xi} = \frac{(f_{i+\frac{1}{2}j} - f_{i-\frac{1}{2}j})}{\Delta \xi} - \frac{(\Delta \xi)^2}{24} f_{\xi\xi\xi}. \tag{20}$$

Similarly the finite difference expression for second-order spatial derivatives is given by

$$\frac{\partial^2 f}{\partial \xi^2} = \frac{(f_{i+1,j} - 2f_{i,j} + f_{i-1,j})}{(\Delta \xi)^2} - \frac{(\Delta \xi)^2}{12} f_{\xi\xi\xi\xi}. \tag{21}$$

The second-order differences for the cross-derivative terms can be expressed as

$$\frac{\partial f}{\partial \xi \partial \eta} = \frac{f_{i+1,j+1} - f_{i-1,j+1} - f_{i+1,j-1} + f_{i-1,j-1}}{4\Delta \xi \Delta \eta} - \frac{1}{6} \left((\Delta \xi)^2 f_{\xi\eta\eta} + (\Delta \eta)^2 f_{\xi\xi\eta} \right). \tag{22}$$

Discretizing the time derivative in the ξ -momentum equation, Eq. (17) gives

$$\begin{aligned} (DU^c)_{ij}^{n+1} = & \frac{1}{1.5} \left\{ 2(DU^c)_{ij}^n - 0.5(DU^c)_{ij}^{n-1} \right\} + \frac{\Delta t^2}{4.5} \left(\frac{\partial^3 (DU^c)}{\partial t^3} \right) - \frac{1}{1.5} \left[\frac{gD}{R \sin^2 \gamma g_{(11)}} \zeta \right]_{\xi} \\ & + \frac{1}{1.5} \left[\frac{gDA \cos \gamma}{R \sin^2 \gamma g_{(22)}} \zeta \right]_{\eta}. \end{aligned} \tag{23}$$

The total truncation error in the ξ -momentum equation, after approximating the first derivative terms in Eq. (23), using Eq. (20), is given by

$$TE1 = \frac{\Delta t^2}{4.5} \left(\frac{\partial^3 (DU^c)}{\partial t^3} \right) + \frac{1}{1.5} \left\{ \frac{(\Delta \xi)^2}{24} \left[\frac{\Delta t g D}{R \sin^2 \gamma g_{11}} \zeta \right]_{\xi\xi\xi}^{n+1} \right\} + \frac{1}{1.5} \left\{ -\frac{(\Delta \eta)^2}{24} \left[\frac{\Delta t g D A \cos \gamma}{R \sin^2 \gamma g_{22}} \zeta \right]_{\eta\eta\eta}^{n+1} \right\}. \tag{24}$$

Discretizing the time derivative in the η -momentum equation, Eq. (18) gives

$$\begin{aligned} (DV^c)_{ij}^{n+1} = & \frac{1}{1.5} \left\{ 2(DV^c)_{ij}^n - 0.5(DV^c)_{ij}^{n-1} \right\} + \frac{\Delta t^2}{4.5} \left(\frac{\partial^3 (DV^c)}{\partial t^3} \right) - \frac{1}{1.5} \left[\frac{\Delta t g D \cos \gamma}{R A \sin^2 \gamma g_{(11)}} \zeta \right]_{\xi}^{(n+1)} \\ & + \frac{1}{1.5} \left[\frac{\Delta t g D}{R \sin^2 \gamma g_{(22)}} \zeta \right]_{\eta}^{(n+1)}. \end{aligned} \tag{25}$$

The total truncation error in the η -momentum equation, after approximating the first derivative terms in Eq. (25), using Eq. (20), is given by

$$\begin{aligned}
 \text{TE2} = & \frac{\Delta t^2}{4.5} \left(\frac{\partial^3(DU^c)}{\partial t^3} \right) + \frac{1}{1.5} \left\{ \frac{(\Delta \xi)^2}{24} \left[\frac{\Delta t g D \cos \gamma}{R A \sin^2 \gamma g_{(11)}} \zeta \right]_{\xi \xi \xi}^{n+1} \right\} \\
 & + \frac{1}{1.5} \left\{ - \frac{(\Delta \eta)^2}{24} \left[\frac{\Delta t g D}{R \sin^2 \gamma g_{(22)}} \zeta \right]_{\eta \eta \eta}^{n+1} \right\}.
 \end{aligned} \tag{26}$$

Discretizing the time derivative in the continuity equation, Eq. (4) becomes

$$1.5(\zeta)_{i,j}^{n+1} - 2(\zeta)_{i,j}^n + 0.5(\zeta)_{i,j}^{n-1} + \frac{\Delta t^2}{3} \left(\frac{\partial^3(DU^c)}{\partial t^3} \right) + \frac{1}{R \cos \theta} \frac{1}{J} \left[(JU^c \cos \theta D)_\xi + (JV^c \cos \theta D)_\eta \right] = 0. \tag{27}$$

Through algebraic manipulation, the momentum equations are next substituted into the continuity equation to obtain a Helmholtz equation in terms of the surface elevation [7,15]

$$\begin{aligned}
 (1.5\zeta)_{i,j}^{n+1} + \frac{(\Delta t)^2}{1.5} & \left\{ - \left[\frac{gD}{R g_{(11)} \sin^2 \gamma} \zeta \right]_{\xi \xi} + \left[\frac{A g D \cos \gamma}{R \sin^2 \gamma g_{(22)}} \zeta \right]_{\xi \eta} \right\} \\
 + \frac{(\Delta t)^2}{1.5} & \left\{ - \left[\frac{gD \cos \gamma}{A R g_{(11)} \sin^2 \gamma} \zeta \right]_{\xi \eta} + \left[\frac{gD}{R g_{(22)} \sin^2 \gamma} \zeta \right]_{\eta \eta} \right\} \\
 = 2.0(\zeta)_{i,j}^n - 0.5(\zeta)_{i,j}^{n-1} - \frac{\Delta t}{1.5R} & \left\{ [2DU^c]_\xi^n - [0.5U^c D]_\xi^{n-1} + [2DV^c]_\eta^n - [0.5V^c D]_\eta^{n-1} \right\}.
 \end{aligned} \tag{28}$$

The truncation error, due to the terms on the left-hand side of Eq. (28), is given by

$$\begin{aligned}
 \text{TE3} = & \frac{(\Delta t)^2 (\Delta \xi)^2}{18} \left\{ \left[\frac{gD}{R g_{(11)} \sin^2 \gamma} \zeta \right]_{\xi \xi \xi \xi}^{n+1} - \left[\frac{2A g D \cos \gamma}{R g_{(22)} \sin^2 \gamma} \zeta \right]_{\xi \eta \eta \eta}^{n+1} \right\} \\
 & + \frac{(\Delta t)^2 (\Delta \xi)^2}{18} \left\{ \left[\frac{gD}{R g_{(22)} \sin^2 \gamma} \zeta \right]_{\eta \eta \eta \eta}^{n+1} - \left[\frac{2A g D \cos \gamma}{R g_{(11)} \sin^2 \gamma} \zeta \right]_{\eta \xi \xi \xi}^{n+1} \right\} \\
 & + \frac{(\Delta t)^2}{9} \left\{ (\Delta \xi)^2 \left[\frac{gD \cos \gamma}{R g_{(11)} \sin^2 \gamma} \zeta \right]_{\xi \eta \eta \eta}^{n+1} + (\Delta \eta)^2 \left[\frac{gD \cos \gamma}{R g_{(11)} \sin^2 \gamma} \zeta \right]_{\eta \xi \xi \xi}^{n+1} \right\}.
 \end{aligned} \tag{29}$$

It is seen from Eqs. (24), (26), and (29) that the orthogonal truncation error terms are proportional to $1/\sin^2 \gamma$. The non-orthogonal truncation error in the ξ - and η -momentum equations are, respectively, proportional to $A \cos \gamma / \sin^2 \gamma$ and $\cos \gamma / \sin^2 \gamma$, where A is the aspect ratio and γ is the grid angle. Thus it can be seen that the coefficients of the truncation error increases with decrease in the grid angle or increase in the aspect ratio. The third-order and fourth-order derivative terms appearing in Eqs. (24), (26), and (29) are cumbersome to evaluate numerically.

It is noted that the truncation error in Eq. (29) requires evaluation of fourth-order derivative terms to achieve second-order accuracy in ξ and η . Each fourth-order derivative term, when expressed in a generalized boundary-fitted coordinate system, evaluated using a symbolic program was found to contain more than 100 terms. Appendix A gives the expressions for evaluating the third-order derivative terms, to give an idea of the complexity of the problem.

4. Test cases for studying the effect of grid non-orthogonality

Two test cases, (i) the oscillation of a standing wave in a closed rectangular basin and (ii) tidally forced flow in a channel open at one end, are used to study the effect of non-orthogonality on model predictions. Keeping the number of grid cells the same, the boundary points in the longitudinal direction, away from the left and right boundaries, are moved to generate grids with varying skewness, keeping the spacing of the grid control points uniform, to the extent possible. The length and width of the basin are, respectively, 23,000 and 2244 m. Since the finite difference approximations for the spatial, second derivative, and cross-derivative terms in Helmholtz equation require a 3×3 stencil, five nodes were chosen in the direction of latitude. Fig. 2 shows grids with uniform skewnesses for a grid spacing of 561 m. Grids with uniform skewnesses of 90° , 60° , 50° , and 30° and grid spacings of 2090.9, 1095.2, 561, and 277.1 m were used. The results obtained using these grids are compared with the corresponding analytical solution. In this study the skewness angle for a given grid has been maintained for most of the domain, except near the boundaries. The non-uniformity of the grid occurring near the boundaries could not be avoided for the grids used in this study.

4.1. Standing wave in a closed rectangular basin

The analytical solutions for surface elevation and velocity for a standing wave in a closed rectangular basin are given by:

$$\zeta(x, t) = a \cos kx \cos \sigma t, \quad (30)$$

$$u(x, t) = \frac{aC}{h} \sin kx \sin \sigma t, \quad (31)$$

where a is the maximum amplitude, $k = 2\pi/L$, $\sigma = 2\pi/T$, and $C = \sqrt{gh}$, L is the wavelength, T is the period, and h is the depth of water. The length of the basin l is taken to be 23,000 m and the depth h is 10 m. The wavelength and the fundamental seiching period (T) for the problem are 46,000 m and 4647 s, respectively.

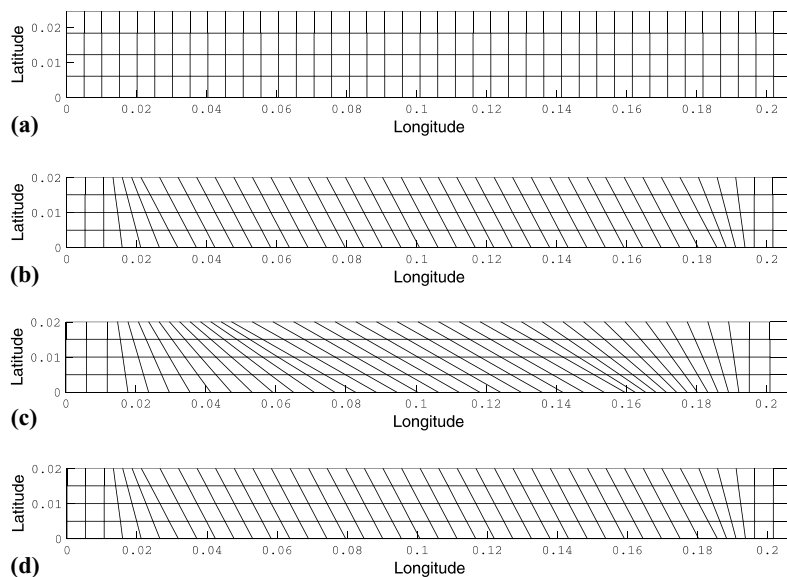


Fig. 2. Grid with a angle of: (a) $\gamma = 90^\circ$, $dx = dy = 561$ m; (b) $\gamma = 61^\circ$, $dx = dy = 561$ m; (c) $\gamma = 50^\circ$, $dx = dy = 561$ m; (d) $\gamma = 30^\circ$, $dx = dy = 561$ m.

The initial water surface profile was one-half of a cosine wave with a maximum at the left end and a minimum at the right end. The amplitude a of the initial cosine wave is set at 0.1 m, with a amplitude to basin depth ratio of 0.01, to minimize the potential for nonlinear effects. The velocities U (along channel) and V (cross-channel) are initialized as zero at $t = 0$. Since three time levels are employed, the initial water surface profile (corresponding to $t = 0$) is forced at the n th and $(n - 1)$ th time steps. A time step of 60 s is used. The grid spacing and gridpoints/wavelength in the longitudinal direction and the Courant number for the different grids are given in Table 1.

Fig. 3(a) shows a comparison of the time series of model predicted surface elevation with the analytical solution, near the left end of the basin, for a grid spacing of $\Delta x = 561$ m with different grid angles. Fig. 3(b)

Table 1
Grid resolution for the seiche oscillation case

Grid spacing	Grid points per wavelength	Courant number
2090.9	22	0.28
1095.2	42	0.54
561	82	1.06
277.1	166	2.14

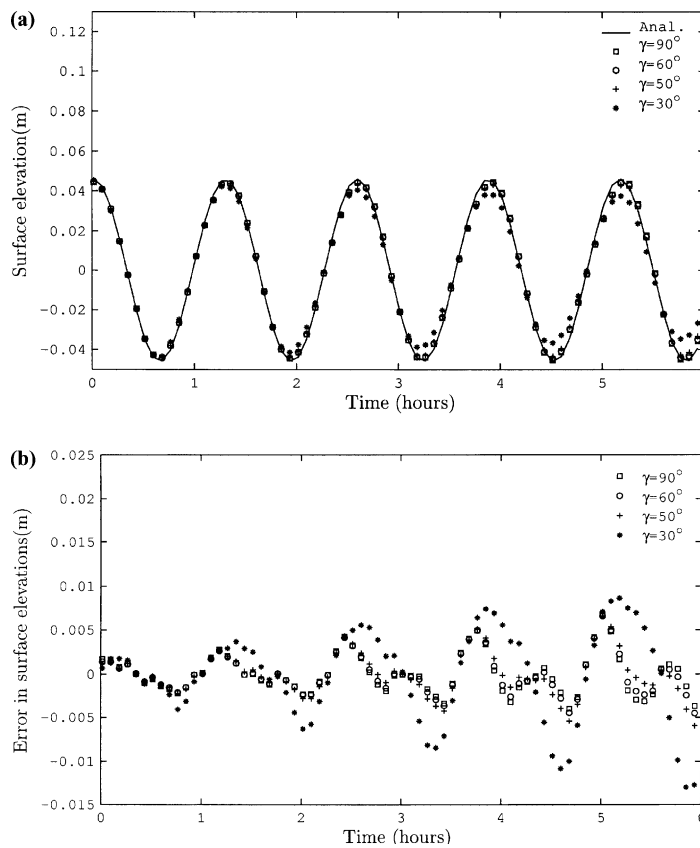


Fig. 3. (a) Comparison of model predicted surface elevations with analytical solution at $x = 8000$ m from the left end of the basin for the seiching case with different grid angles, $\Delta t = 60$ s, $\Delta x = 561$ m, $h = 10$ m, and $L = 46,000$ m. (b) Relative error of model predicted elevations with analytical solution $x = 8000$ m from the left end of the basin for the seiching case with different grid angles, $\Delta t = 60$ s, $\Delta x = 561$ m, $h = 10$ m, and $L = 46,000$ m.

shows the relative difference in surface elevation between analytical and numerical solutions. The maximum percentage error in the peak amplitude of the surface elevation after three cycles, for a grid angle of 30° is found to be 22%, compared to 15% error for grid angles above 50° . Fig. 4(a) shows a comparison of the time series of the model predicted velocities with analytical solution for a grid spacing of $\Delta x = 561$ m for different grid angles and Fig. 4(b) shows the relative error between the two. The maximum percentage error in the peak amplitude of the velocities for a grid with a grid angle of 30° was found to be 20%, compared to 5% error for grids with grid angles above 50° . Model predictions of surface elevations and velocities using a time step of 6 s for a grid with a non-orthogonality angle of 30° did not improve the results. A gradual growth of higher harmonics was seen after three cycles (not shown), which has also been reported by Leendertse et al. [17], while using an explicit scheme and by Leendertse [18], while using an implicit scheme. The longitudinal velocities were found to be constant across a section, independent of the grid angle. Transverse velocities of the order of 10^{-3} m/s were found to develop for a grid having an angle of 30° .

The effect of grid resolution and grid angle on the solution is studied by comparing the Root Mean Square (RMS) error between the model prediction and analytical solution for the grids.

The variations of the RMS error in surface elevations and velocities with grid angle and grid resolution are shown, respectively, in Figs. 5(a) and (b). The RMS errors in model predicted surface elevations and

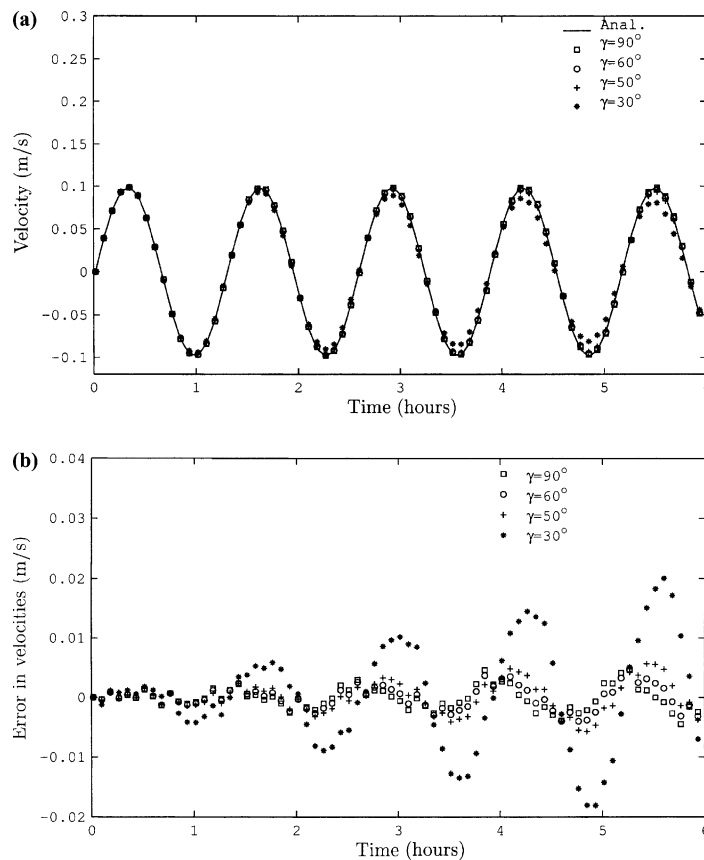


Fig. 4. (a) Comparison of model predicted U -velocities with analytical solution at $x = 8000$ m from the left end of the basin for the seiching case with different grid angles, $\Delta t = 60$ s, $\Delta x = 561$ m, $h = 10$ m, and $L = 46,000$ m. (b) Relative error of model predicted U -velocities with analytical solution at $x = 8000$ m from the left end of the basin for the seiching case with different grid angles, $\Delta t = 60$ s, $\Delta x = 561$ m, $h = 10$ m, and $L = 46,000$ m.

velocities are found to increase gradually, as the grid resolution decreases from 166 to 22 gridpoints per wavelength or as the grid angle decreases from 90° to 50° and increases rather sharply for a grid angle of 30° at resolutions less than 80 gridpoints per wavelength.

4.2. Tidal forcing in a rectangular channel open at one end

A comparison of model predictions with the analytical solution [19] is performed for the case of tidally forced flow in a channel open at the right end, for grids with different grid angles. A cosine tidal forcing, given by $\zeta(x, t) = a \cos \sigma t$, is applied at the right end of the channel. The origin of the x -axis is taken at the left end of the channel, corresponding to the reflection point for the standing wave, for which the velocity is zero for all time. The open boundary is at $x = 23,000$ m.

Following [19], the analytical solutions for the surface elevation and velocity are given by

$$\zeta(x, t) = \frac{a}{\cos kl} \cos kx \cos \sigma t, \tag{32}$$

$$u(x, t) = \frac{aC}{h \cos kl} \sin kx \sin \sigma t, \tag{33}$$

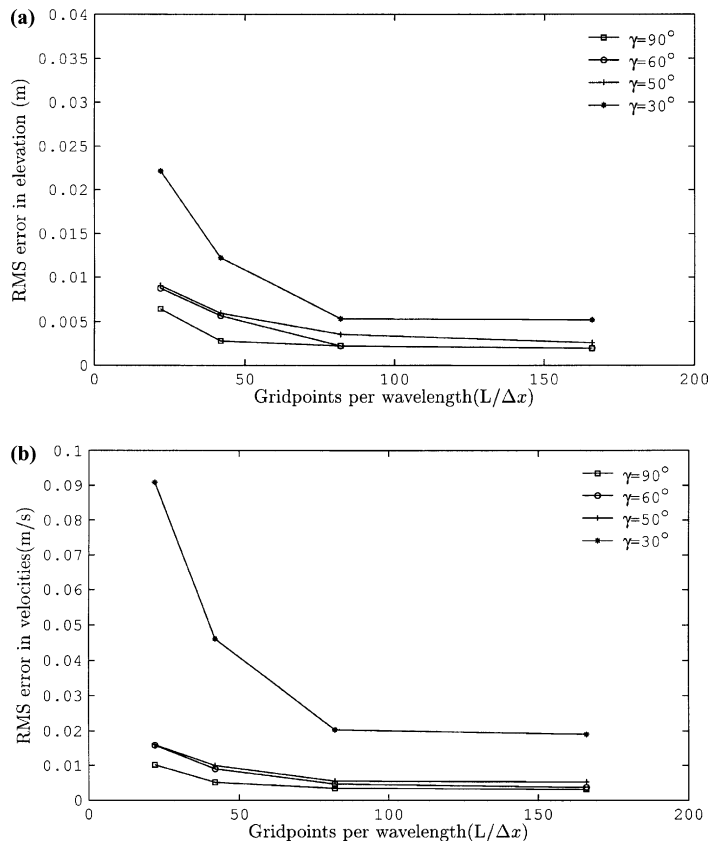


Fig. 5. (a) RMS error in elevations versus gridpoints per wavelength at $x = 8000$ m from the left end. (b) RMS error in velocities versus gridpoints per wavelength versus at $x = 8000$ m from the left end.

Table 2
Grid resolution for the tidal forcing case

Grid points per wavelength	Wavelength (m)	Period (h)
1400	2.93020E + 06	82.18
1200	2.51160E + 06	70.44
1000	2.09300E + 06	58.70
800	1.67440E + 06	46.96
600	1.25580E + 06	35.22
400	8.37200E + 05	23.48
300	6.27900E + 05	17.61
250	5.23250E + 05	14.67
200	4.18600E + 05	11.74
175	3.66275E + 05	10.27
150	3.13950E + 05	8.80
125	2.61625E + 05	7.34
110	2.30230E + 05	6.46
100	2.09300E + 05	5.87

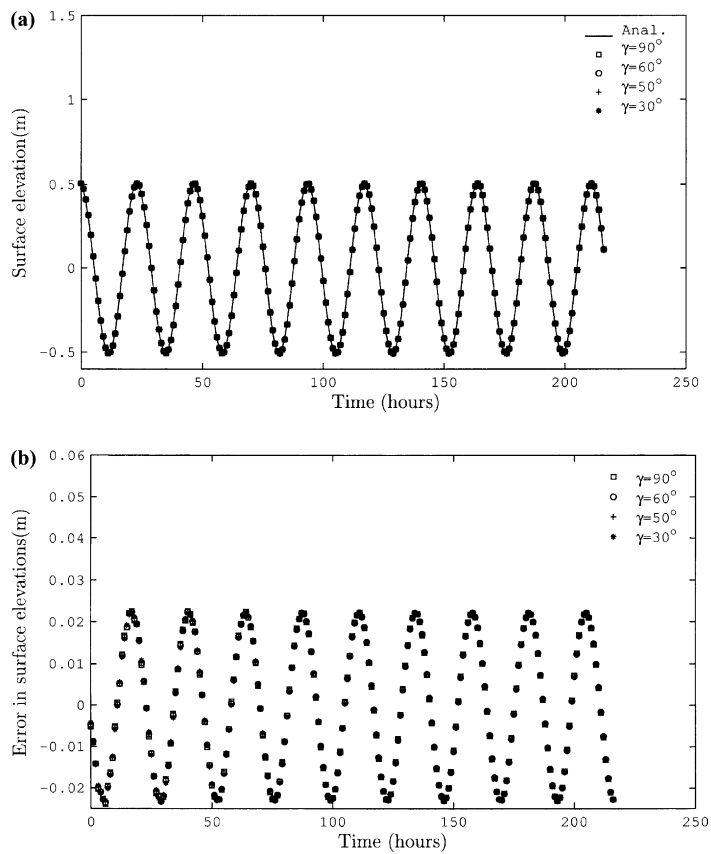


Fig. 6. (a) Comparison of model predicted surface elevations with analytical solution at the center of the basin for the tidal forcing case with $\Delta t = 10$ min, $\Delta x = 561$ m, $T = 23.5$ h, $L = 837.2$ km, and $h = 10$ m. (b) Relative error of model predicted elevations with analytical solution at the center of the basin for the tidal forcing case with $\Delta t = 10$ min, $\Delta x = 561$ m, $T = 23.5$ h, $L = 837.2$ km, and $h = 10$ m.

where $C = \sqrt{gh}$, C is the wave celerity (or wave speed), h is the depth of the basin, and x is the distance from the origin.

The following values are used in the numerical solution: $l = 23,000$ m, $h = 10$ m, $\Delta t = 10$ min, $\Delta x = 561$ m, where a is the amplitude at the open end of the basin, h is the water depth, Δt is the time step, and Δx is the space step. The Courant number is 10.6. Table 2 gives the periods, wavelength, and gridpoints per wavelength for cases studied, for a water depth of $h = 10$ m.

Fig. 6(a) shows a comparison of model predicted surface elevation with the analytical solution, near the center of the basin, for a tidal period of $T = 23.5$ h, for grids with different angles of non-orthogonality. Fig. 6(b) shows the relative error in surface elevation between the two solutions. The maximum percentage error in the peak amplitude of surface elevation is found to be 4.4%, even for grids having an grid angle as low as 30° . It is observed that the model predicted surface elevations are insensitive to the grid angle (γ). Fig. 7(a) shows a comparison of the velocities from the analytical and numerical solutions, at the center of the basin, and at the second grid point from the southern boundary in the cross-stream direction. Fig. 7(b) shows the relative error between two. It is seen that the percentage error in the peak amplitude of the velocities is found to be less than 5% for grid angles greater than 50° and increases sharply to 12% as the grid angle decreases to 30° .

The effect of grid resolution and grid angle on the solution is studied by comparing the RMS error between the model predictions and the analytical solution for a 10-day period, varying the tidal forcing

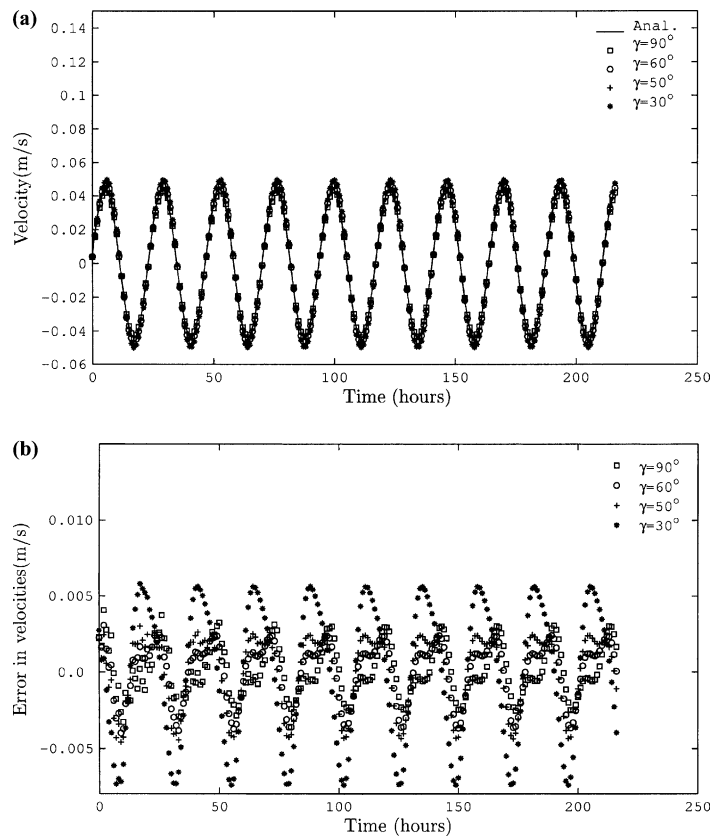


Fig. 7. (a) Comparison of model predicted U -velocities with analytical solution at the center of the basin and at the second gridpoint from the southern boundary for the tidal forcing case with $\Delta t = 10$ min, $\Delta x = 561$ m, $L = 837.2$ km, $h = 10$ m, and $T = 23.5$ h. (b) Relative error of model predicted velocities with analytical solution at the center of the basin and at the second gridpoint from the southern boundary for the tidal forcing case with $\Delta t = 10$ min, $\Delta x = 561$ m, $L = 837.2$ km, $h = 10$ m, and $T = 23.5$ h.

period at the open boundary for the grids shown in Fig. 2. Fig. 8 shows that the RMS error in surface elevation is insensitive to the grid angle for grids with grid resolutions greater than 600 gridpoints per wavelength. The RMS error is found to increase gradually as the grid resolution decreases from 600 to 200 gridpoints per wavelength or as the grid angle decreases from 90° to 30° . The RMS error in surface elevation is found to increase sharply for grid resolutions less than 200 gridpoints per wavelength or as the grid angle decreases from 90° to 30° .

Fig. 9 shows that the RMS error in velocities at $x = 11,500$ m from the left end and at the first gridpoint from the southern boundary is found to increase gradually as the grid angle decreases from 90° to 30° or as the grid resolution decreases from 1400 to 400 gridpoints per wavelength. The RMS error in velocities increases sharply with the decrease in grid angle for grid resolutions less than 400 gridpoints per wavelength. It was seen that the RMS error in velocities at $x = 11,500$ m from the left end and at the second gridpoint from the southern boundary exhibits a pattern similar to that at the first gridpoint from the southern boundary, except that the RMS errors are less in this case. The higher RMS error at the boundaries can be attributed to the one sided difference used at the boundaries. The RMS error in velocities at the right end near the open boundary is not sensitive to the grid angle, as the grids are not skewed near

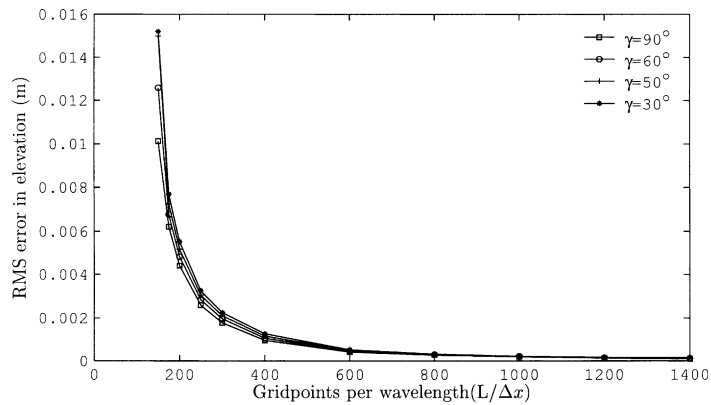


Fig. 8. RMS error of the surface elevations versus gridpoints per wavelength at the center and at the first gridpoint from the southern boundary.

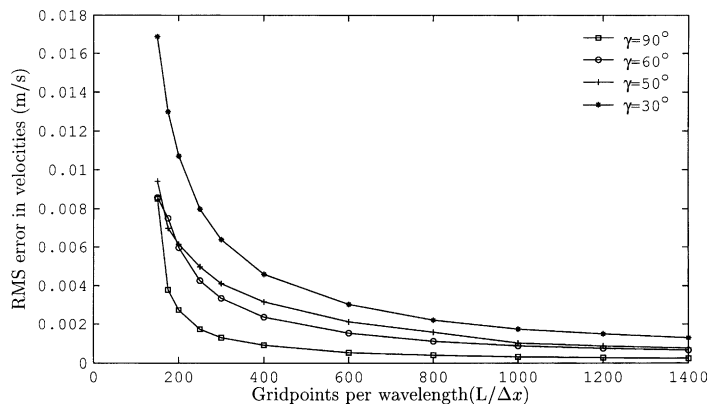


Fig. 9. RMS error of the velocities versus gridpoints per wavelength at the center and at the first gridpoint from the southern boundary.

the right end. It is thus seen that the error due to the non-orthogonality of the grid is localized. The RMS errors are found to increase gradually as the grid resolution decreases from 1400 to 400 gridpoints per wavelength and sharply for grid resolutions less than 400 gridpoints per wavelength.

The model predicted surface elevations and velocities are insensitive to the grid angle for grid resolutions greater than 600 gridpoints per wavelength. The error in model predicted velocities are found to increase as the grid resolution decreases from 1400 to 400 gridpoints per wavelength or as the grid angle decreases from 90° to 30° .

5. Effect of grid angle on the hydrodynamic modeling in Narragansett Bay

The effect of grid angle on the hydrodynamic circulation in Narragansett Bay is studied using three different boundary-fitted grid configurations. The bathymetry of Narragansett Bay is shown in Fig. 10. The mean depth of the bay is 8.3 m. An overview of the hydrodynamic circulation in Narragansett Bay is given in Gordon and Spaulding [20]. The boundary-fitted grid for the study area is shown in Fig. 11. A very fine grid resolution (Fig. 12) is used in Greenwich Bay, located in the western side of the Narragansett Bay, to compare the model predicted currents with the observed currents at the mouth of the Greenwich Bay. The major advantages of a generalized non-orthogonal boundary-fitted grid in fitting the coastal boundaries appropriately in the narrow coves are clearly shown in Fig. 12. The grid size ranges from 75 to 750 m and consists of 4480 grid cells. Depth data (Fig. 10) for the area were derived from the NOAA bathymetric

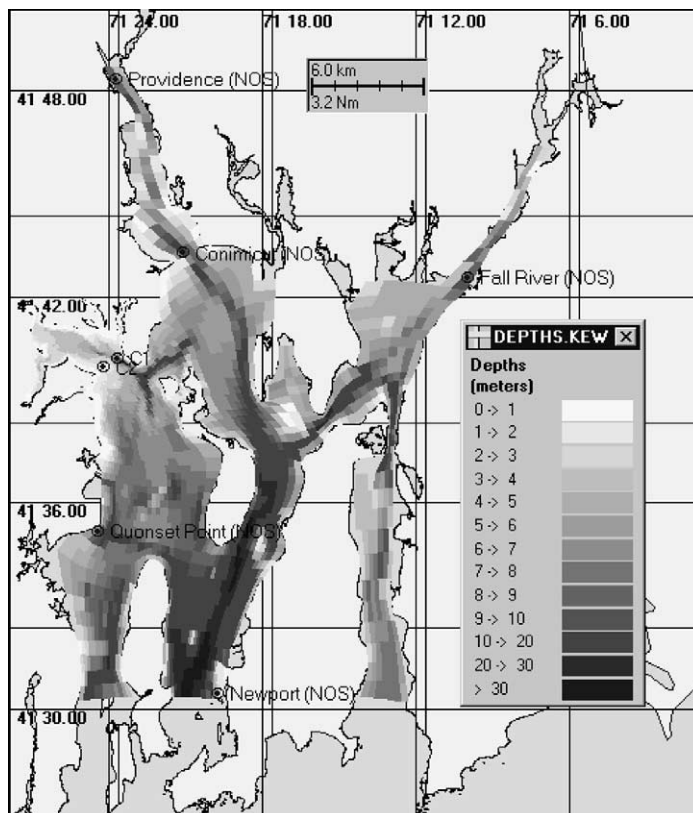


Fig. 10. Narragansett Bay study area and its bathymetric contours.

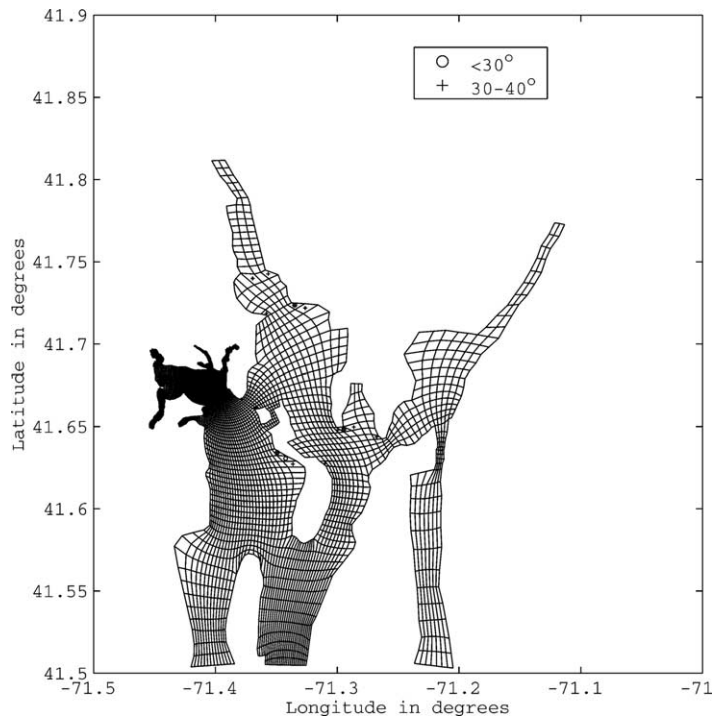


Fig. 11. Grid configuration for the Narragansett Bay (Grid1) (unpublished D. Mendelsohn, Applied Science Associates).

charts for Narragansett Bay. Data were mapped to provide a mean depth for each boundary-fitted grid cell in the study area.

Table 3 gives a summary of the number of grid cell corners for various grid angles in those ranges for three different grids, Grid1, Grid2, and Grid3, used in this study. Grid2 (not shown in the figures) was constructed as a variation of Grid1, but with grid angles less than 40° and Grid3 is constructed as a very coarse grid. It can be seen from Table 3 that 95% of the grid cells have grid angles above 60° . A two-dimensional vertically averaged hydrodynamic model simulation of flow in Narragansett Bay was performed using the three grids. The convective, coriolis, and baroclinic terms were neglected and a quadratic bottom friction coefficient of 0.0035 determined by Spaulding et al. [21] was used. The observed sea surface elevation at 6 min intervals, at the National Ocean Service (NOS) station at Newport [22] was used as a forcing at the southern boundary of the grid at Newport (Fig. 10). The model predicted surface elevations compares well with the observed surface elevations using Grid1 [22] at Quonset Point, Conimicut point, Fall River and Providence (Figs. 13(a)–(d)). The RMS error between the observed and predicted surface elevation using the three grids, at the four NOS stations for a 60-day period for the three grids is shown in Table 4. It is seen that the model predicted surface elevations are insensitive to the grid quality parameters. It is known that the 85% of the tidal energy of the tides in Narragansett Bay is concentrated on M2 tide, which has a period of 12.42 h. A single S4 current meter deployed at mid-depth at station C1 (Fig. 10) by Applied Science Associates [23] is used to compare the model predicted currents. An S4 current meter measures current speed, direction, wave, tide, turbidity, and water quality parameters [23]. The model predicted U and V velocities for the grid, grid1 at station C1, compare well with the observed data as shown in Figs. 14(a) and (b).

Taking the approximate length of the study area as 35 km and the depth to be 8.3 m, the wavelength of the M2 tidal wave propagating into the Narragansett Bay works out to be 420 km. The grid spacing used

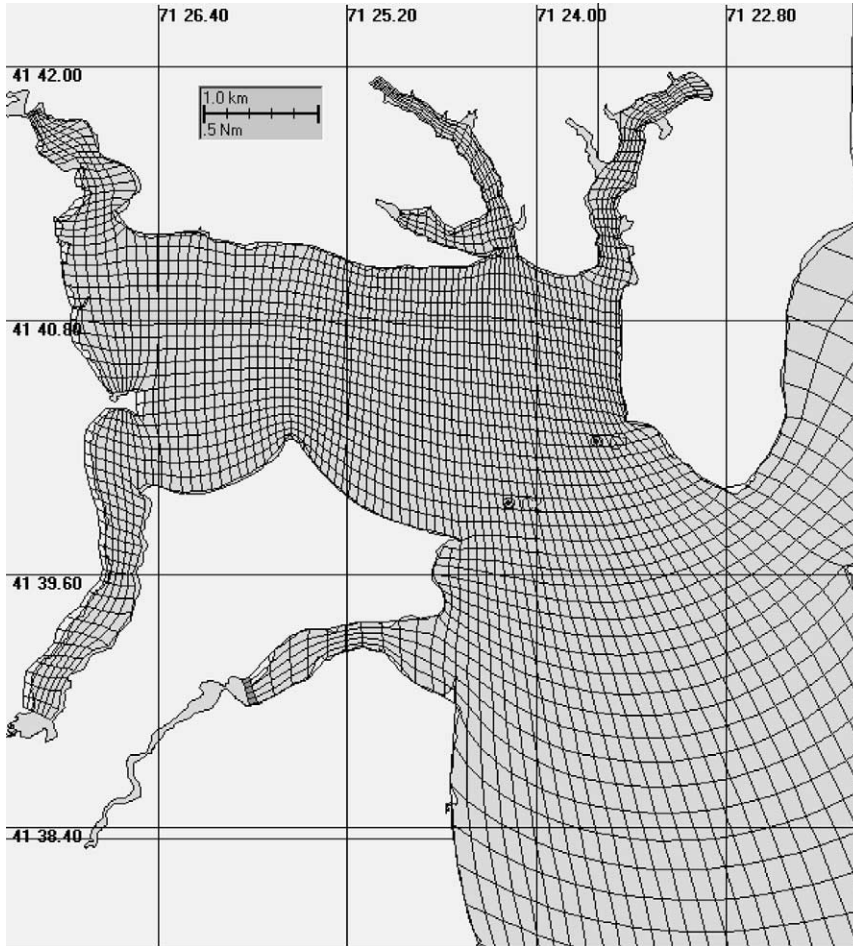


Fig. 12. Detail of the Grid (Grid1) in Greenwich Bay.

Table 3
Range of grid angles for the Narragansett Bay grid

Range of γ	Number of grid cell corners		
	Grid1	Grid2	Grid3
0–30°	19	0	0
30–40°	56	0	3
40–50°	197	92	6
50–60°	751	631	19
60–70°	2072	2111	46
70–80°	6093	6157	179
80–90°	8492	8479	575

for the grid ranges from 750 to 75 m and the corresponding grid resolution ranges from 5600 to 560 gridpoints per wavelength and this grid resolution is found to be adequate for modeling the tidal circulation in Narragansett Bay and hence the model predictions are found to be insensitive to the grid angle.

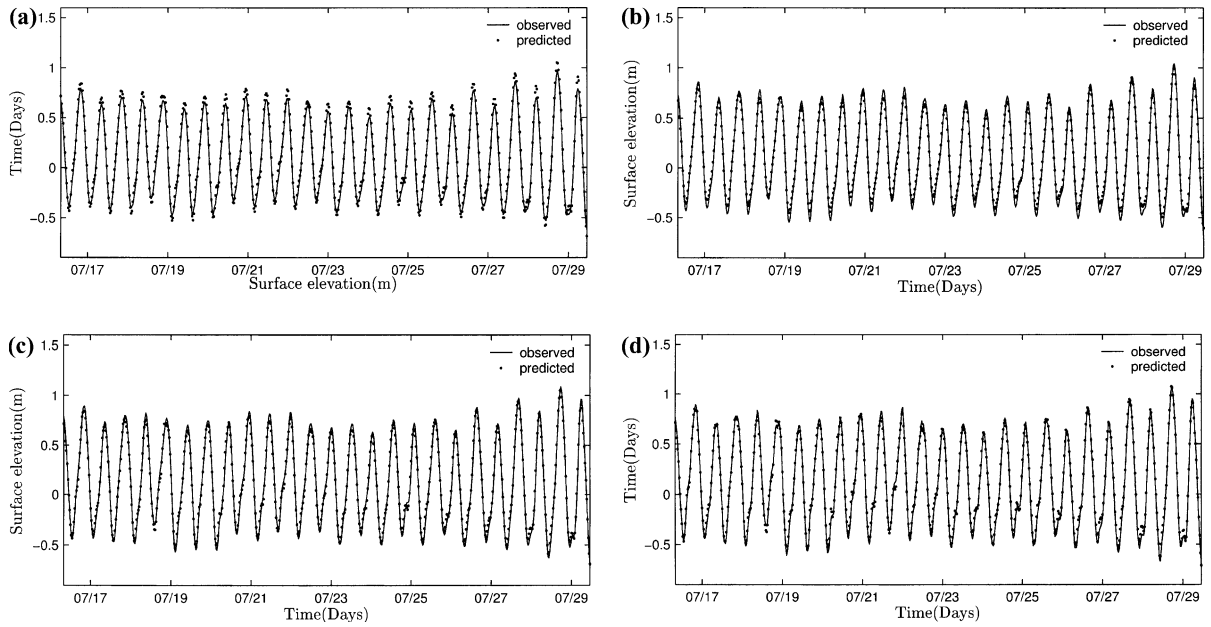


Fig. 13. Comparison of observed and predicted surface elevations in: (a) Quonset point; (b) Conimicut point; (c) Fall River; (d) Providence.

Table 4
The RMS error between observed and predicted surface elevations at the NOAA/NOS stations

Station	RMS error (m)		
	Grid1	Grid2	Grid3
Conimicut	0.058	0.058	0.059
Quonset	0.063	0.063	0.063
Fall River	0.070	0.069	0.070
Providence	0.063	0.062	0.063

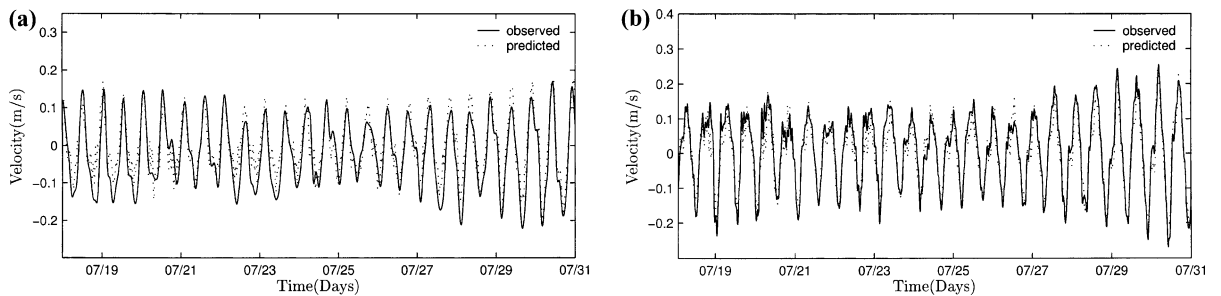


Fig. 14. (a) Comparison of observed and model predicted U -velocities at C1 station. (b) Comparison of observed and model predicted V -velocities at C1 station.

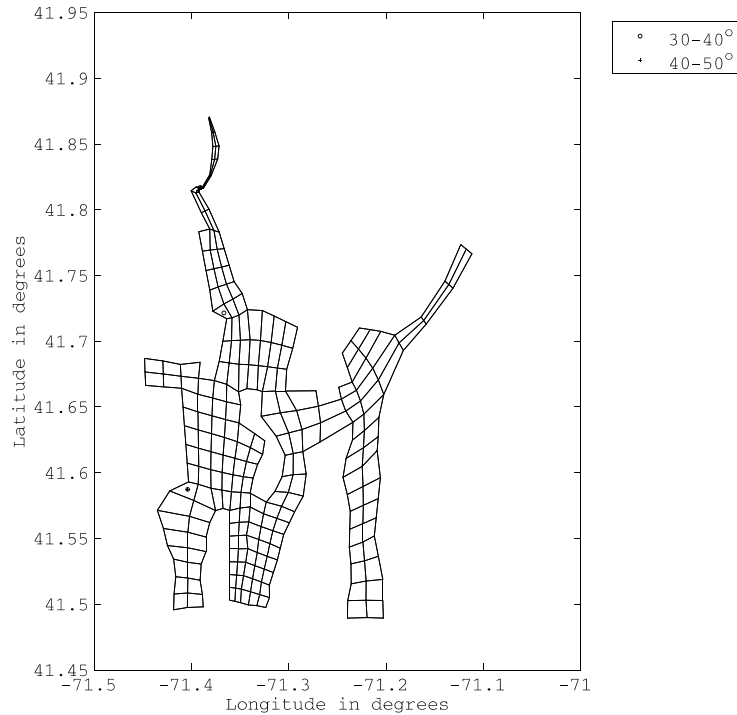


Fig. 15. Coarse grid configuration for the Narragansett Bay (Grid3).

Table 5
The RMS error between observed and predicted velocities at C1 station

Station	RMS error (m/s)		
	Grid1	Grid2	Grid3
<i>U</i> -velocity	0.042	0.042	0.056
<i>V</i> -velocity	0.034	0.033	0.040

To study the effect of grid resolution on the model predictions, a coarse grid (Grid3), shown in Fig. 15 with grid spacing ranging from 1300 to 2000 m, is used. The grid resolution for grid3 works out to be 200–310 for the M2 tide and the RMS error in model predicted surface elevations is found to be insensitive to the grid spacing, even at this grid resolution as shown in Table 5. However, the RMS error in model predicted velocities is found to increase by at least 1 cm/s for coarse grid, when compared to the fine grid.

6. Conclusions

Results of the truncation error analysis show that the truncation error terms due to first and second derivative terms are functions of grid angle and aspect ratio. The coefficient of the truncation error was shown to increase, with the decrease in the grid angle or increase in the aspect ratio.

The RMS errors in surface elevation and velocities for the case of seiche in a rectangular basin are found to increase gradually as the grid resolution decreases from 166 to 22 gridpoints per wavelength or as

the grid angle decreases from 90° to 50°. The RMS error in model predicted velocities are found to increase sharply as the grid resolution decreases for grid with a grid angle of 30°.

The model predicted surface elevations for the case of tidal forcing in a rectangular channel are found to be insensitive to the grid angle at resolutions higher than 600 grids per wavelength. The error in model predicted velocities are found to increase as the grid resolution decreases from 1400 to 400 gridpoints per wavelength or as the grid angle decreases from 90° to 30°. The RMS error in model predicted velocities are found to be more pronounced for low grid angle near the boundaries and this can be attributed to the one-sided difference near the boundaries. The grid angle dependence evident in the model predicted velocities, but not seen in the surface elevation can be attributed to the fact that the velocities are transformed into the computational plane.

A two-dimensional modeling of tidal circulation in Narragansett Bay using three different grids confirmed that the model predicted surface elevations are insensitive to the grid angle at grid resolutions ranging from 500 to 200 gridpoints per wavelength. However, the RMS errors in model predicted currents were found to increase by 1 cm/s as the grid resolution decreases from 600 to 200 gridpoints per wavelength.

We conclude from this study that the grid angle and grid resolution affects the accuracy of the model predicted currents and the numerical dispersion increases with the decrease in grid angle or grid resolution and these are in agreement with the conclusions reached by Sankaranarayanan and Spaulding [2] through a Fourier analysis of the discretized equations in boundary-fitted coordinates.

Acknowledgements

The first author wishes to thank the University of Rhode Island (URI) for providing him a Graduate fellowship for a year. Part of the study was also sponsored by the URI Sea Grant Program. The authors wish to thank the Applied Science Associates Inc. for allowing us to use their WQMAP software to generate the grid systems used in this study. Discussions with Dan Mendelsohn are gratefully acknowledged. Thanks are also due to the three anonymous reviewers and Dr. P.K. Smolarkiewicz, for their critical comments.

Appendix A

This section gives the expressions needed to evaluate the truncation errors TE1, TE2, and TE3 appearing in Eqs. (24), (26), and (29).

The first derivatives of function f with respect to ξ and η can be expressed using Eqs. (A.1) and (A.2)

$$f_{\xi} = f_{\theta}\theta_{\xi} + f_{\phi}\phi_{\xi}, \quad (\text{A.1})$$

$$f_{\eta} = f_{\theta}\theta_{\eta} + f_{\phi}\phi_{\eta}. \quad (\text{A.2})$$

The first derivative of function f with respect to ϕ and θ can be evaluated using Eqs. (A.3) and (A.4)

$$f_{\phi} = (f_{\xi}\theta_{\eta} - f_{\eta}\theta_{\xi})/J, \quad (\text{A.3})$$

$$f_{\theta} = (f_{\eta}\phi_{\xi} - f_{\xi}\phi_{\eta})/J. \quad (\text{A.4})$$

The second derivatives of function f with respect to ξ and η and the cross-derivatives of function f with respect to ξ and η can be expressed using Eqs. (A.5)–(A.7)

$$f_{\xi\xi} = f_{\theta}\theta_{\xi\xi} + f_{\phi}\phi_{\xi\xi} + \theta_{\xi}(f_{\theta\theta}\theta_{\xi} + f_{\phi\theta}\phi_{\xi}) + \phi_{\xi}(f_{\phi\theta}\theta_{\xi} + f_{\phi\phi}\phi_{\xi}), \quad (\text{A.5})$$

$$f_{\eta\eta} = f_{\theta}\theta_{\eta\eta} + f_{\phi}\phi_{\eta\eta} + \theta_{\eta}(f_{\theta\theta}\theta_{\eta} + f_{\phi\theta}\phi_{\eta}) + \phi_{\eta}(f_{\phi\theta}\theta_{\eta} + f_{\phi\phi}\phi_{\eta}), \tag{A.6}$$

$$f_{\xi\eta} = (f_{\theta\theta}\theta_{\eta} + f_{\phi\theta}\phi_{\eta})\theta_{\xi} + \phi_{\xi}(f_{\phi\theta}\theta_{\eta} + f_{\phi\phi}\phi_{\eta}) + f_{\theta}\theta_{\eta\xi} + f_{\phi}\phi_{\eta\xi}. \tag{A.7}$$

The second derivatives of function f with respect to ϕ and θ and the cross-derivatives of function f with respect to ϕ and θ can expressed using Eqs. (A.8)–(A.10)

$$\begin{aligned} f_{\phi\phi} = & \left\{ (f_{\xi}\phi_{\eta} - f_{\eta}\phi_{\xi})(\theta_{\eta})^2\theta_{\xi\xi} + f_{\eta}\phi_{\eta\eta}(\theta_{\xi})^3 - f_{\xi}\phi_{\xi\xi}(\theta_{\eta})^3 \right\} / J^3 + \left\{ [(f_{\xi}\phi_{\eta} - f_{\eta}\phi_{\xi})\theta_{\eta\eta} \right. \\ & - (f_{\xi}\phi_{\eta\eta} + 2f_{\eta}\phi_{\eta\xi})\theta_{\eta}] (\theta_{\xi})^2 \left. \right\} / J^3 - \left\{ [(f_{\eta}\phi_{\xi} + f_{\xi}\phi_{\eta})2\theta_{\eta}\theta_{\eta\xi} + (f_{\eta}\phi_{\xi\xi} + 2f_{\xi}\phi_{\eta\xi})(\theta_{\eta})^2] \theta_{\xi} \right\} / J^3 \\ & + \left\{ f_{\xi\xi}(\theta_{\eta})^2 + f_{\eta\eta}(\theta_{\xi})^2 - 2f_{\eta\xi}\theta_{\eta}\theta_{\xi} \right\} / J^2, \end{aligned} \tag{A.8}$$

$$\begin{aligned} f_{\theta\theta} = & \left\{ [f_{\eta}(\phi_{\eta})^2\phi_{\xi\xi} + f_{\eta}\phi_{\eta\eta}(\phi_{\xi})^2 - 2f_{\eta}\phi_{\eta}\phi_{\eta\xi}\phi_{\xi}] \theta_{\xi} \right\} / J^3 + \left\{ [f_{\eta}(\phi_{\xi})^3 - f_{\xi}\phi_{\eta}(\phi_{\xi})^2] \theta_{\eta\eta} \right. \\ & + [2f_{\xi}(\phi_{\eta})^2\phi_{\xi} - 2f_{\eta}\phi_{\eta}(\phi_{\xi})^2] \theta_{\eta\xi} \left. \right\} / J^3 - \left\{ [f_{\xi}(\phi_{\eta})^2\phi_{\xi\xi} + f_{\xi}\phi_{\eta\eta}(\phi_{\xi})^2 - 2f_{\xi}\phi_{\eta}\phi_{\eta\xi}\phi_{\xi}] \theta_{\eta} \right. \\ & + f_{\eta\eta}J(\phi_{\xi})^2 \left. \right\} / J^3 + \left\{ -2f_{\eta\xi}J\phi_{\eta}\phi_{\xi} + f_{\xi\xi}J(\phi_{\eta})^2 + [f_{\xi}(\phi_{\eta})^3 - f_{\eta}(\phi_{\eta})^2\phi_{\xi}] \theta_{\xi\xi} \right\} / J^3, \end{aligned} \tag{A.9}$$

$$\begin{aligned} f_{\phi\theta} = & \left\{ [f_{\eta}\phi_{\eta}\phi_{\xi} - f_{\xi}(\phi_{\eta})^2] \theta_{\eta}\theta_{\xi\xi} + (f_{\eta}\phi_{\eta}\phi_{\eta\xi} - f_{\eta}\phi_{\eta\eta}\phi_{\xi})(\theta_{\xi})^2 \right\} / J^3 + \left\{ [f_{\eta}(\phi_{\xi})^2 - f_{\xi}\phi_{\eta}\phi_{\xi}] \theta_{\eta\eta}\theta_{\xi} \right. \\ & + [f_{\xi}(\phi_{\eta})^2 - f_{\eta}\phi_{\eta}\phi_{\xi}] \theta_{\eta\xi}\theta_{\xi} \left. \right\} / J^3 + \left\{ [(f_{\xi}\phi_{\eta\eta} + f_{\eta}\phi_{\eta\xi})\phi_{\xi} - (f_{\xi}\phi_{\eta\xi} + f_{\eta}\phi_{\xi\xi})\phi_{\eta}] \theta_{\eta}\theta_{\xi} \right\} / J^3 \\ & + \left\{ [f_{\xi}\phi_{\eta}\phi_{\xi} - f_{\eta}(\phi_{\xi})^2] \theta_{\eta}\theta_{\eta\xi} + (f_{\xi}\phi_{\eta}\phi_{\xi\xi} - f_{\xi}\phi_{\eta\xi}\phi_{\xi})(\theta_{\eta})^2 \right\} / J^3 + \left\{ (2f_{\eta\xi}\phi_{\xi}\theta_{\eta} - f_{\xi\xi}\phi_{\eta})\theta_{\eta} \right. \\ & - f_{\eta\eta}\phi_{\xi}\theta_{\xi} - f_{\eta\xi}J \left. \right\} / J^2. \end{aligned} \tag{A.10}$$

The third derivatives of function f with respect to ξ and η and the cross-derivatives of function f with respect to ξ and η can expressed using Eqs. (A.11)–(A.14)

$$\begin{aligned} f_{\xi\xi\xi} = & \theta_{\xi}[f_{\theta\theta}\theta_{\xi\xi} + \theta_{\xi}(f_{\theta\theta\theta}\theta_{\xi} + f_{\phi\theta\theta}\phi_{\xi}) + \phi_{\xi}(f_{\phi\theta\theta}\theta_{\xi} + f_{\phi\phi\theta}\phi_{\xi}) + f_{\phi\theta}\phi_{\xi\xi}] \\ & + \phi_{\xi}[f_{\phi\theta}\theta_{\xi\xi} + \phi_{\xi}(f_{\phi\phi\theta}\theta_{\xi} + f_{\phi\phi\phi}\phi_{\xi}) + \theta_{\xi}(f_{\phi\theta\theta}\theta_{\xi} + f_{\phi\phi\theta}\phi_{\xi}) + f_{\phi\phi}\phi_{\xi\xi}] \\ & + 2\theta_{\xi\xi}(f_{\theta\theta}\theta_{\xi} + f_{\phi\theta}\phi_{\xi}) + 2\phi_{\xi\xi}(f_{\phi\theta}\theta_{\xi} + f_{\phi\phi}\phi_{\xi}) + f_{\theta}\theta_{\xi\xi\xi} + f_{\phi}\phi_{\xi\xi\xi}, \end{aligned} \tag{A.11}$$

$$\begin{aligned} f_{\xi\xi\eta} = & \theta_{\xi}[(f_{\theta\theta\theta}\theta_{\eta} + f_{\phi\theta\theta}\phi_{\eta})\theta_{\xi} + f_{\theta\theta}\theta_{\eta\xi} + \phi_{\xi}(f_{\phi\theta\theta}\theta_{\eta} + f_{\phi\phi\theta}\phi_{\eta}) + f_{\phi\theta}\phi_{\eta\xi}] \\ & + \phi_{\xi}[(f_{\phi\theta\theta}\theta_{\eta} + f_{\phi\phi\theta}\phi_{\eta})\theta_{\xi} + f_{\phi\theta}\theta_{\eta\xi} + \phi_{\xi}(f_{\phi\phi\theta}\theta_{\eta} + f_{\phi\phi\phi}\phi_{\xi}) + f_{\phi\phi}\phi_{\eta\xi}] \\ & + \theta_{\eta\xi}(f_{\theta\theta}\theta_{\xi} + f_{\phi\theta}\phi_{\xi}) + \phi_{\eta\xi}(f_{\phi\theta}\theta_{\xi} + f_{\phi\phi}\phi_{\xi}) + \phi_{\xi\xi}(f_{\phi\theta}\theta_{\eta} + f_{\phi\phi}\phi_{\eta}) \\ & + f_{\theta}\theta_{\eta\xi\xi} + f_{\phi}\phi_{\eta\xi\xi} + (f_{\theta\theta}\theta_{\eta} + f_{\phi\theta}\phi_{\eta})\theta_{\xi\xi}, \end{aligned} \tag{A.12}$$

$$\begin{aligned} f_{\xi\eta\eta} = & [f_{\theta\theta}\theta_{\eta\eta} + \theta_{\eta}(f_{\theta\theta\theta}\theta_{\eta} + f_{\phi\theta\theta}\phi_{\eta}) + \phi_{\eta}(f_{\phi\theta\theta}\theta_{\eta} + f_{\phi\phi\theta}\phi_{\eta}) + f_{\phi\theta}\phi_{\eta\eta}]\theta_{\xi} \\ & + \phi_{\xi}[f_{\phi\theta}\theta_{\eta\eta} + \phi_{\eta}(f_{\phi\phi\theta}\theta_{\eta} + f_{\phi\phi\phi}\phi_{\eta}) + \theta_{\eta}(f_{\phi\theta\theta}\theta_{\eta} + f_{\phi\phi\theta}\phi_{\eta}) + f_{\phi\phi}\phi_{\eta\eta}] \\ & + 2(f_{\theta\theta}\theta_{\eta} + f_{\phi\theta}\phi_{\eta})\theta_{\eta\xi} + 2\phi_{\eta\xi}(f_{\phi\theta}\theta_{\eta} + f_{\phi\phi}\phi_{\eta}) + f_{\phi}\phi_{\eta}\eta_{\xi\xi} + f_{\theta}\theta_{\eta\eta\xi}, \end{aligned} \tag{A.13}$$

$$\begin{aligned}
f_{\eta\eta} = & \theta_{\eta} [f_{\theta\theta}\theta_{\eta\eta} + \theta_{\eta}(f_{\theta\theta\theta}\theta_{\eta} + f_{\phi\theta\theta}\phi_{\eta}) + \phi_{\eta}(f_{\phi\theta\theta}\theta_{\eta} + f_{\phi\phi\theta}\phi_{\eta}) + f_{\phi\theta}\phi_{\eta\eta}] \\
& + \phi_{\eta} [f_{\phi\theta}\theta_{\eta\eta} + \phi_{\eta}(f_{\phi\phi\theta}\theta_{\eta} + f_{\phi\phi\phi}\phi_{\eta}) + \theta_{\eta}(f_{\phi\theta\theta}\theta_{\eta} + f_{\phi\phi\theta}\phi_{\eta}) + f_{\phi\phi}\phi_{\eta\eta}] \\
& + 2\theta_{\eta\eta}(f_{\theta\theta}\theta_{\eta} + f_{\phi\theta}\phi_{\eta}) + 2\phi_{\eta\eta}(f_{\phi\theta}\theta_{\eta} + f_{\phi\phi}\phi_{\eta}) + f_{\theta}\theta_{\eta\eta\eta} + f_{\phi}\theta_{\eta\eta\eta}.
\end{aligned} \tag{A.14}$$

References

- [1] M. Muin, M.L. Spaulding, Two-dimensional boundary-fitted circulation model in spherical coordinates, *J. Hydraul. Eng.-ASCE* 122 (9) (1996) 512.
- [2] S. Sankaranarayanan, M.L. Spaulding, in: Dispersion and stability analyses of shallow water equations in boundary-fitted coordinates, Department of Ocean Engineering, University of Rhode Island, 2001, p. 33.
- [3] J.J. Wanstrath, Nearshore numerical storm surge and tidal simulation model, T.R. H-77-17, U.S. Army Engineer Water Ways Experiment Station, Vicksburg, MS, 1977, p. 51.
- [4] A.F. Blumberg, H.J. Herring, Circulation modeling in orthogonal curvilinear coordinates, in: J.C.J. Nihoul, B.M. Jamarat (Eds.), *Three-dimensional Models of Marine and Estuarine Dynamics*, 1987, p. 629.
- [5] Y.P. Sheng, A three-dimensional model of coastal, estuarine and lake currents using boundary-fitted grid, Technical Report No. 585, Aeronautical Research Associates of Princeton, Princeton, NJ, 1983, p. 41.
- [6] M.L. Spaulding, A vertically averaged circulation model using boundary-fitted coordinates, *J. Phys. Oceanography* 14 (1984) 973.
- [7] J.C. Swanson, A three-dimensional numerical model system of coastal circulation and water quality. Ph.D. Thesis, Ocean Engineering, University of Rhode Island, Kingston, RI, 1986, p. 147.
- [8] J.F. Thompson, Z.U.A. Warsi, C.W. Mastin, in: *Numerical Grid Generation – Foundations and Applications*, North-Holland, New York, 1985, p. 482.
- [9] H.G. Hauser, D. Paap, D. Eppel, A. Mueller, Solution of Shallow Water Equations for complex flow domains using boundary-fitted coordinates, *Int. J. Numer. Meth. Fluids* 5 (1987) 727.
- [10] A.G.L. Borthwick, G.A. Akponasa, Reservoir flow prediction by contravariant shallow water equations, *J. Hydraul. Eng.-ASCE* 123 (5) (1997) 432.
- [11] C.W. Mastin, Error Induced by coordinate systems, pp. 31–40, in: J.F. Thompson (Ed.), *Proceedings of the Conference on Numerical Grid Generation*, North-Holland, New York, 1982, p. 909.
- [12] D.G. Kerlick, G.H. Klopfer, Assessing the quality of curvilinear coordinate meshes by decomposing the Jacobian matrix, in: J.F. Thompson (Ed.), *Numerical Grid Generation*, North-Holland, New York, 1982, p. 909.
- [13] Per Nielson, O. Skovgaard, The effect of using non-orthogonal boundary-fitted grids for solving shallow water equation, *Int. J. Numer. Meth. Fluids* 11 (1990) 177.
- [14] D. Lee, Y.M. Tsuei, A formula for the estimation of truncation errors of convective terms in a curvilinear coordinate system, *J. Comput. Phys.* 98 (1992) 90.
- [15] R.V. Madala, S.A. Piasek, A semi implicit numerical model for Baroclinic oceans, *J. Comput. Phys.* 23 (1977) 1167.
- [16] A. Arakawa, V.R. Lamb, Computational design of the basic dynamical processes of the ULCA General Circulation Model, *Meth. Comput. Phys.* 17 (1977) 173.
- [17] J.J. Leendertse, R.C. Alexander, S.K. Liu, Three-dimensional model for estuaries and coastal seas, vol. 1 Principles of computation, Report R-1417-OWRR, Rand Corporation, Santa Monica, CA, 1973, p. 65.
- [18] J.J. Leendertse, A new approach to three-dimensional model free-surface flow modeling, R-3712-NETH/RC, Rand Corporation, Santa Monica, CA, 1989, p. 51.
- [19] A.T. Ippen, in: *Estuarine and Coastline Hydrodynamics*, McGraw Hill, Newyork, NY, 1966, p. 744.
- [20] R.B. Gordon, M.L. Spaulding, Numerical simulations of tidal and wind-driven circulation in Narragansett Bay, *Estuarine, Coastal Shelf Sci.* 1987 24 (1987) 611.
- [21] M.L. Spaulding, S. Sankaranarayanan, L. Erikson, T. Fake, T. Opishinski, COASTMAP, An integrated system for monitoring and modeling of coastal waters: application to Greenwich bay, in: M.L. Spaulding, A.F. Blumberg (Eds.), *Proceedings of the 5th International Conference on Estuarine and Coastal Modeling*, ASCE, Alexandria, VA, 1998, p. 870.
- [22] NOAA/NOS. Available from <http://www.co-ops.nos.noaa.gov> [10th August 2001].
- [23] Applied Science Associates Final data report for: Greenwich Bay water quality sampling, Summer 2000, RP 00-29, 2001, p. 80.
- [24] J. Pedlosky, in: *Geophysical Fluid Dynamics*, Springer, New York, 1987, p. 710.